INTERFACE

rsif.royalsocietypublishing.org

Research

Cite this article: Hornung R, Grünberger A, Westerwalbesloh C, Kohlheyer D, Gompper G, Elgeti J. 2018 Quantitative modelling of nutrient-limited growth of bacterial colonies in microfluidic cultivation. *J. R. Soc. Interface* **15**: 20170713.
http://dx.doi.org/10.1098/rsif.2017.0713

Received: 29 September 2017
Accepted: 22 January 2018

Subject Category:
Life Sciences–Physics interface

Subject Areas:
biophysics

Keywords:
nutrient gradients, bacterial nutrient consumption, growth simulations, microfluidic cultivation

Author for correspondence:
Jens Elgeti
e-mail: j.elgeti@fz-juelich.de

Quantitative modelling of nutrient-limited growth of bacterial colonies in microfluidic cultivation

Raphael Hornung[1,†], Alexander Grünberger[2,3,†], Christoph Westerwalbesloh[2], Dietrich Kohlheyer[2,4], Gerhard Gompper[1] and Jens Elgeti[1]

[1]Theoretical Soft Matter and Biophysics, Institute of Complex Systems and Institute for Advanced Simulation, Forschungszentrum Jülich and JARA, 52425 Jülich, Germany
[2]Institute of Bio- and Geosciences, IBG-1: Biotechnology, Forschungszentrum Jülich, 52425 Jülich, Germany
[3]Multiscale Bioengineering, Bielefeld University, Universitätsstrasse 25, Bielefeld 33615, Germany
[4]Aachener Verfahrenstechnik (AVT.MSB), RWTH Aachen University, 52056 Aachen, Germany

RH, 0000-0002-6729-7289; AG, 0000-0002-7564-4957; CW, 0000-0002-3064-7425; DK, 0000-0001-6215-1857; GG, 0000-0002-8904-0986; JE, 0000-0001-7300-0923

Nutrient gradients and limitations play a pivotal role in the life of all microbes, both in their natural habitat as well as in artificial, microfluidic systems. Spatial concentration gradients of nutrients in densely packed cell configurations may locally affect the bacterial growth leading to heterogeneous micropopulations. A detailed understanding and quantitative modelling of cellular behaviour under nutrient limitations is thus highly desirable. We use microfluidic cultivations to investigate growth and microbial behaviour of the model organism *Corynebacterium glutamicum* under well-controlled conditions. With a reaction–diffusion-type model, parameters are extracted from steady-state experiments with a one-dimensional nutrient gradient. Subsequently, we employ particle-based simulations with these parameters to predict the dynamical growth of a colony in two dimensions. Comparing the results of those simulations with microfluidic experiments yields excellent agreement. Our modelling approach lays the foundation for a better understanding of dynamic microbial growth processes, both in nature and in applied biotechnology.

1. Introduction

Growth of cells is enabled by diffusive factors, a property which is universal for all living processes ranging from growth of single bacteria [1,2] or eukaryotic cells [3,4] to tissue [5–8] and biofilm formation [9–12]. There is a complex interplay between diffusion and uptake, strongly influenced by metabolism and environment. Typically, various environmental perturbations—such as nutrient gradients, oxygen depletion, temperature changes and others—occur simultaneously, rendering the analysis of nutrient limitations and their influence on individual cellular systems challenging. Microfluidic cultivation systems—which often consist of microfluidic growth chambers with well-controlled nutrient supply—are ideal to analyse and quantify cellular behaviour under defined environmental conditions [13,14]. They facilitate the investigation of single selected limiting factors while keeping others in a defined range [15,16]. Furthermore, microfluidic cultivation enables observation of cellular growth patterns by microscopy with a high spatio-temporal resolution. This combination allows quantitative modelling and parameter extraction. Whereas most microfluidic studies so far have used undefined or defined but non-limiting conditions for the cultivation, only few studies have artificially limited cell growth within microfluidic devices [17–19]. To understand how nutrient limitation affects growth patterns, we investigate the growth of the bacterium *Corynebacterium glutamicum*, a non-motile bacterial model organism, at different distinct carbon-source

---

[†]These authors contributed equally to this study.

Electronic supplementary material is available online at https://dx.doi.org/10.6084/m9.figshare.c.3991626.

THE ROYAL SOCIETY
PUBLISHING

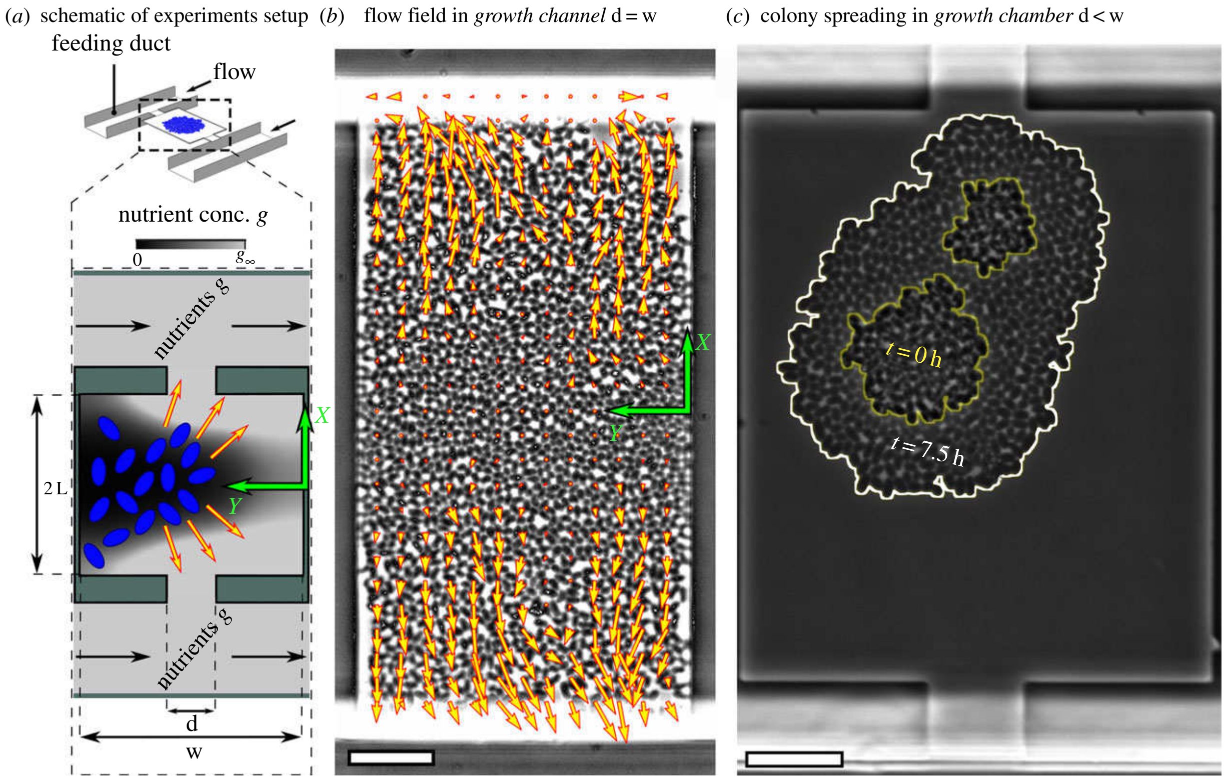

Figure 1. Microfluidic set-up. (*a*) Schematic of microfluidic experiment in which *Corynebacterium glutamicum* are grown. The microfluidic device provides constant nutrient supply by the flow in the large feeding ducts; g_∞ denotes the feeding concentration. Inside the chamber the bacteria (blue) take up the nutrients, the local concentration g drops and nutrient gradients occur (greyscale depicting local concentration). The bacteria grow and a flow towards the channel outlets evolves (red–yellow arrows). (*b*) Snapshot of the *growth channel* set-up used to observe the steady-state flowfield of bacteria. Overlaid vectors depict the flowfield of bacteria inside the channel, as measured by particle image velocimetry (PIV). Scale bar, 10 µm. (*c*) Overlay of two snapshots at different time points of an experiment in a *growth chamber* with narrow outlets to study the spreading dynamics of a bacterial colony. The yellow and white lines depict the perimeter of the colony at different time points. Scale bar, 10 µm.

concentrations. Our microfluidic system [20] acts as a 'quasi'-chemostat and allows the investigation of growing microcolonies in a two-dimensional monolayer under well-defined environmental conditions (figure 1). In a first step, we grow cells in a quasi-one-dimensional set-up, i.e. a wide and open *growth channel* (figure 1*b*). We derive a minimal theoretical model for growth which we fit to the steady-state motion pattern of cells for a single experimental condition. Our colony-growth model allows a direct read-off of the nutrient-uptake function from experimental data; the results show good agreement with Monod [21] and Teissier [22] nutrient-uptake functions. With the fit we extract the length scale of nutrient depletion within a colony and the nutrient dependency of growth. In a second step, we extrapolate to other feeding concentrations. Encouraged by excellent agreement, in a third step we extrapolate from this steady-state, quasi-one-dimensional geometry to the prediction of time-dependent growth of bacteria in a genuine two-dimensional set-up (*growth chamber*, figure 1*c*). To do so, we feed the fitted parameters into a particle-based growth simulation [23] and compare the shape and area of growing colonies over time. The simulations show striking agreement with growth dynamics observed experimentally, demonstrating the predictive power of our minimal modelling approach. Currently, measurements of concentration profiles on the microscale are unfeasible. Our findings close this gap by providing a way to quantify nutrient distributions from the measurable velocity profile. Furthermore, our results serve as a basis for the design of optimized microfluidic systems for microbial cultivation.

2. Results and discussion

2.1. Theory for nutrient uptake and biomass conversion

Cells need to metabolize nutrients in order to grow. The amount of nutrients taken up depends on the concentration $g = \hat{g}\bar{g}$ of nutrients available, where we introduce the dimensionless concentration $\hat{g}$ and the unit conversion factor $\bar{g}$. Furthermore, it is reasonable to assume that the nutrient-uptake rate u per bacterium has an upper bound $u_\infty\bar{g}$. Hence, we write the total nutrient-uptake rate per bacterium as $u_\infty\bar{g}u(\hat{g})$, where $u(\hat{g})$ is a dimensionless function varying between zero and unity. The nutrient concentration field $\hat{g}$ thus obeys

$$\partial_t\hat{g} = D\Delta\hat{g} - \varrho u_\infty u(\hat{g}), \tag{2.1}$$

where we assume the uptake to be linear in bacterial number density ϱ and only diffusive nutrient transport [18] with diffusion constant D. Bacteria convert the nutrients absorbed into biomass with efficiency ϵ, i.e. cells grow with a rate of $k = \epsilon u_\infty u(\hat{g})$. Thus, the bacterial density evolves according to

$$\partial_t\varrho = -\nabla\cdot(\varrho \boldsymbol{v}) + \varrho\epsilon u_\infty u(\hat{g}), \tag{2.2}$$

with the bacteria flow velocity $\boldsymbol{v}$. The efficiency parameter ϵ describes essentially the amount of nutrients a bacterium needs to consume in order to divide. Similar reaction–diffusion-type models have also been used, for example, to investigate velocity and shape of bacterial growth fronts [24] or the growth behaviour of bacterial aggregates [25].

For constant bacterial density and fast diffusion, these equations simplify to

$$\Delta\hat{g} = \frac{u(\hat{g})}{l_g^2} \quad \text{and} \quad \nabla\cdot\boldsymbol{v} = \epsilon u_\infty u(\hat{g}), \tag{2.3}$$

with two parameters, the nutrient decay length $l_g = \sqrt{D/\varrho u_\infty}$ describing the ratio of nutrient-uptake rate to diffusive nutrient flux, and the maximum growth rate $k_{\max} = \epsilon u_\infty$. Furthermore, the shape of the uptake function $u(\hat{g})$ determines at which nutrient-concentration scale limitation of growth occurs. The exact uptake rate as a function of nutrient availability $u(\hat{g})$ is generally not known; however, in one dimension, model equations (2.3) can be rearranged to read off u from a given velocity profile $v(x)$. For a quasi-one-dimensional colony of length $2L$, with prescribed nutrient concentration $\hat{g}(\pm L) = \hat{g}_\infty$ at the boundaries, elimination of $u(\hat{g})$ from equations (2.3) yields

$$\hat{g}(x) = \frac{V(x) - V_0}{k_{\max} l_g^2}, \tag{2.4}$$

where $V(x) = \int_{x_0}^{x} v(x')\,\mathrm{d}x'$ the integral of v starting from the flow symmetry axis $x = x_0$ (at which $g'(x_0) = v(x_0) = 0$) and $V_0 = k_{\max} l_g^2 \hat{g}(x_0)$. Insertion of equation (2.4) into equation (2.3) eliminates the nutrient concentration, so that

$$\frac{\mathrm{d}v}{\mathrm{d}x} = k_{\max} u\left(\frac{V(x) - V_0}{k_{\max} l_g^2}\right). \tag{2.5}$$

Thus, the shape of the uptake function $u(\hat{g})$, and the scalar parameters l_g and $k_{\max}$ can be extracted from a fit of our model to experimental results for a quasi-one-dimensional system, as will be discussed below.

2.2. Growth channel experiments with *Corynebacterium glutamicum*

We investigated the growth of *C. glutamicum* in a quasi-one-dimensional *growth channel* geometry (figure 1*a*,*b*) to facilitate modelling and interpretation of growth patterns. To prevent co-metabolism of different carbon sources [26], modified CGXII medium without glucose was used as the growth medium. Here protocatechuic acid (PCA) served as the sole carbon source and growth limiting factor. We performed growth channel experiments with four different concentrations in the feeding duct (figure 1*a*): $g_\infty = 48.75\,\mu\mathrm{M}$ ($n = 2$ independent experiments), $97.5\,\mu\mathrm{M}$ ($n = 3$), $390\,\mu\mathrm{M}$ ($n = 3$) and $585\,\mu\mathrm{M}$ ($n = 4$) PCA in aqueous solution. Time-lapse phase contrast microscopy images of the growing microcolonies were recorded every $\Delta t = 5$–10 min over 40 h of microfluidic cultivation to follow the growth on different feeding levels. Starting from a few bacteria seeded into the growth channel, bacteria grow, divide and populate all available space in the growth channel. Bacteria are pushed out of the channel into the feeding duct and are dragged away by the flow. Finally, a continuous steady state evolves which is characterized by the balanced growth and outflow of bacteria (see the electronic supplementary material, movie M1). Nutrient limitation was clearly visible for the lowest feeding concentrations $48.75\,\mu\mathrm{M}$ and $97.5\,\mu\mathrm{M}$ where we observed an almost complete growth arrest in ≈2/3 of the growth channel (see the electronic supplementary material, movie M2). This decline of growth activity clearly demonstrates the presence of nutrient gradients which develop on a length scale of a few cell sizes. At the same time, for the highest feeding concentration $585\,\mu\mathrm{M}$ ($n = 2$), no growth arrest zones were visible and bacterial biomass production took place along the whole channel length, paralleled by a strong flow of cells towards the channel outlets. For the intermediate feeding concentration of $390\,\mu\mathrm{M}$, we observed a mixed picture: the flow was clearly much stronger than for the lowest feeding concentration, but a small fraction close to the chamber centre exhibited low to no growth. To quantify the observed growth patterns, we analysed the flow patterns $\boldsymbol{v} = (v_x, v_y)$ using PIV [27] (see Material and methods). In the steady state, we observed a plug-like flow with almost no dependence of the velocity on the y-position. To compare the velocity profile with our theory, we define $v(x)$ as the average of v_x along the y-direction and over all steady-state time points. Resulting velocity profiles v for the different feeding levels are shown in figure 2*a*. The growth arrest zones are clearly visible. At the channel outlets, PIV underestimates the velocity due to (i) bacteria being washed out of the channel such that the correlation with the next frame often fails and (ii) because velocity and frequency of division events increase, both of which raise the difficulty of a correct correlation match. Thus, the velocity decrease close to the channel outlets and the corresponding maxima are artefacts. We decided to limit our quantitative analysis to a central region of the channel heuristically defined as the interval between the two inflection points closest to the two maxima at the channel outlets ($x_\pm$; figure 2*a*–*c*, vertical dashed-dotted lines). We also checked the sensitivity of our results to include all data points up to the velocity maxima near the channel outlets and found only minor deviations.

2.3. Matching continuum model and experiments

We commence our analysis with the estimation of a suitable uptake function u from our velocity data. Relation (2.5) predicts that a $\mathrm{d}v/\mathrm{d}x - V$-plot of our measured velocity profiles collapses onto the uptake function u if each curve is shifted along the V-axis by an offset $V_0 = k_{\max} l_g^2 \hat{g}(x_0)$ proportional to the concentration at the starting point x_0 of the integration (figure 3). An initial guess for the shifts V_0^i is obtained easily by visual inspection, because continuity demands that datasets for $\mathrm{d}v/\mathrm{d}x - V$ from different experiments have to overlap. Different models for uptake kinetics [21,22] agree on a set of conditions:

$$\text{linear for small concentrations } u(\hat{g}) \overset{\hat{g}\to 0}{\propto} \hat{g}, \tag{2.6}$$

$$\text{saturating at high concentrations } u(\hat{g}) \overset{\hat{g}\to\infty}{\longrightarrow} 1, \tag{2.7}$$

$$\text{monotonically increasing } u' > 0 \tag{2.8}$$

$$\text{and} \quad \text{concave everywhere, i.e. } u'' < 0. \tag{2.9}$$

which are also consistent with our data. We choose the unit conversion factor $\bar{g}$ such that the linear slope for small concentrations in condition (2.6) is equal to unity. Thus, the length scale l_g describes the exponential decay length of the nutrient concentration under limiting conditions, where $u(\hat{g}) \approx \hat{g}$. Conditions (2.6) and (2.7) imply a simple geometrical interpretation of the parameters $k_{\max}$ and l_g in the $\mathrm{d}v/\mathrm{d}x - V$-plane. From equation (2.5) and condition (2.6), it follows $\mathrm{d}v/\mathrm{d}x \overset{\hat{g}\to\infty}{=} (V - V_0^i)/l_g^2$, equation (2.5) and condition (2.7) yield $\mathrm{d}v/\mathrm{d}x \overset{\hat{g}\to\infty}{=} k_{\max}$. Hence, $k_{\max}$ and l_g fix the initial slope

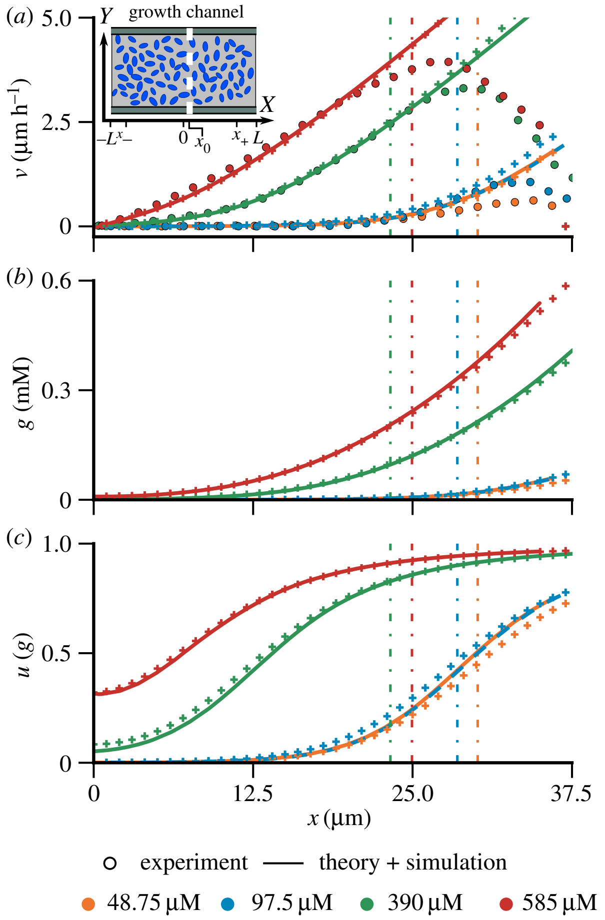

Figure 2. Velocity and the nutrient concentration profile in growth channel set-up. (*a*) Velocity profiles estimated by PIV of growth channel experiments and subsequent averaging over the *y*-direction and time (circles). One example for each feeding concentration g_∞ is shown, as indicated in the legend (see the electronic supplementary material, figure S1 for all data). Owing to the symmetry of the velocity profile with respect to the channel centre, the *x*-range from the channel centre to the feeding outlets is displayed. The flow symmetry axis position x_0 has also been fitted to account for small deviations from the channel centre at $x = 0$. Dashed-dotted vertical lines indicate the cut-off x_+ used to constrain the data range used for the fit to our analytic model equations (2.3) (for details of fit see Material and methods). Continuous lines show the velocity profiles of the model fit using Monod uptake which has been extrapolated towards the channel outlets. The line for the concentration $g_\infty = 48.75$ is dashed to increase visibility. Flow profiles of corresponding particle-based simulations are shown with '$+$'-symbols. Experimental and simulation data have been averaged over time and along the *y*-direction. (*b–c*) *g*- and *u*(*g*)-profiles from model fit (continuous lines) and corresponding particle simulation results ('$+$'-symbols).

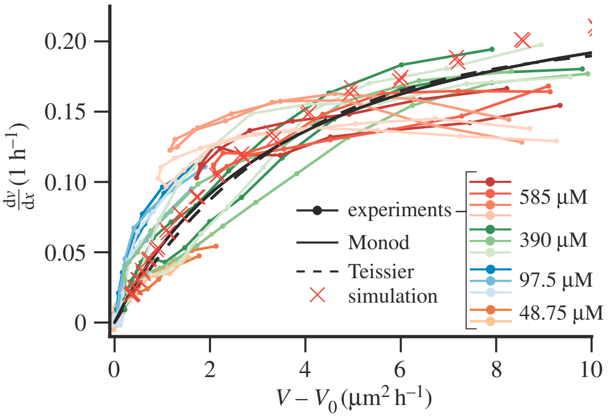

Figure 3. Uptake function extracted from PIV data. A plot of d*v*/d*x* versus $V = \int_{x_0}^{x} v(x')\,\mathrm{d}x'$, the integral of *v* starting from the flow symmetry axis at $x = x_0$, for different nutrient concentrations g_∞, as indicated in the legend. Curves of the different experiments *i* have been shifted by $V_0^i = k_{\max} l_g^2 \hat{g}^i(x_0)$ according to equation (2.5), where the x_0^i and V_0^i have been estimated by a least-square fit (details of fit described in Material and methods). Black lines show fits with Monod uptake $u = \hat{g}/(1+\hat{g})$ (continuous) and Teissier uptake $u = 1 - \exp(-\hat{g})$ (dashed), the red '$\times$' result of a corresponding particle-based simulation. Experimental and simulation data have been averaged over time and along the *y*-direction.

and the saturation value of the $\mathrm{d}v/\mathrm{d}x - V$-curve. We use two common uptake models which comply with conditions (2.6)–(2.9); Monod uptake $u(\hat{g}) = \hat{g}/(1+\hat{g})$ [21] is explored here (figure 3); the very similar results for Teissier uptake $u(\hat{g}) = 1 - \exp(-\hat{g})$ [22] can be found in electronic supplementary material, figure S2. With a suitable uptake function $u(\hat{g})$ our model, defined by equations (2.3), is complete and the theoretical predictions can be fitted to the experimental data. A direct fit of *u* in the $\mathrm{d}v/\mathrm{d}x - V$ diagram, using equation (2.5) to estimate the parameters $k_{\max}$ and l_g, provides an initial estimate. However, the numbers are error-prone due to the derivative of noisy experimental data. Thus, we fit the solution of equations (2.3) for the velocity profile $v(x)$ to the measured flow profiles with $k_{\max}$ and l_g as fit parameters. To account for small deviations of the velocity symmetry axis position from the channel centre, we employ the concentration at the centre and the centre position as additional fit parameters (see Material and methods for details). Note that in figure 3 the experiments at $g_\infty = 390\ \mu\mathrm{M}$ span almost the full relevant concentration range; thus, flow profiles $v(x)$ are fitted for this concentration and the model is then used to predict the velocity profiles at higher and lower concentrations. Model fits give good predictions of experimental data, even for extrapolations to very different concentrations (figure 2*a*). The corresponding fitted Monod- and Teissier-uptake functions are depicted in figure 3. For the positions *x* outside the interval $x_- \leq x \leq x_+$ used for the fit (figure 2 and electronic supplementary material, figure S1, continuous model curves outside dashed-dotted lines), model predictions agree reasonably well up to the velocity maxima. Our model also predicts the nutrient concentration profile $\hat{g}(x)$ inside the channel (figure 2*b*,*c*); however, we emphasize that our fit procedure does not prescribe the feeding concentrations g_∞ as present in the experiments. Comparison of the feeding concentrations via the linear relation $\hat{g}_\infty = g_\infty/\bar{g}$ thus provides an additional consistency check. Linear fits (figure 5) match well and estimate the conversion factor to $\bar{g} = 0.02\,\mathrm{mM}$ for both Monod and Teissier uptake. Note that the theoretical feeding concentration $\hat{g}_\infty$ is estimated from an extrapolation of the $\hat{g}$-profile to the channel outlets (for details, see Material and methods). Owing to the reduced bacterial density, our model is not strictly valid at the channel outlets; thus, this approach only provides an estimate of the concentration scale $\bar{g}$. We define the concentration scale $g_{1/2}$ as the nutrient concentration at which uptake and growth rates are half of their maximum values, thus for $\hat{g}_{1/2}$ it holds $u(\hat{g}_{1/2}) = 1/2$. With the concentration scale $\bar{g}$, we estimate $g_{1/2}$ for Monod and Teissier uptake around $g_{1/2} \approx 13-20\ \mu\mathrm{M}$, which is about 5–10% of the PCA concentration in standard CGXII medium; much lower than we previously assumed for Monod kinetics ($g_{1/2} = 100\ \mu\mathrm{M}$) [18,26]. Our

Table 1. Fit results for model parameters obtained from a least-squares minimization. Error ranges refer to the square-root of the diagonal entries of the covariance matrix, as reported by `least_squares()`.

uptake	k_{max} (h^{-1})	l_g (μm)	$g_{1/2}$ (μM)
Monod	0.26 ± 0.06	3.78 ± 0.17	19.9 ± 1.5
Teissier	0.20 ± 0.03	4.18 ± 0.14	13.6 ± 0.9

observed maximal growth rate of around $k_{max} \approx 0.2 - 0.26\,h^{-1}$ agrees well with previous observations [26]. The nutrient decay length of $l_g \approx 3.8 - 4.2\,\mu m$ falls in the range of $l_g \approx 2$–$5\,\mu m$ which can be estimated from previous results [26], which are affected, however, by large uncertainties. In particular, the conversion of uptake rates measured per gram cell dry weight (g_{CDW}) into uptake per single cell is prone to large errors, because reported single-cell weights vary by an order of magnitude [18]. However, it is important to emphasize that the parameter estimates of previous studies [26] were based on the assumption of spatial homogeneity. Our main result here is that nutrient gradients are very important and have to be considered. Thus, it is no surprise that estimates differ, and we deem the approach of the present study to be more reliable (see table 1 for all fit results).

2.4. Spreading dynamics of *C. glutamicum*

We adapted a particle-based simulation technique for growing tissues [23] to quantitatively predict bacterial growth and nutrient distribution inside arbitrarily shaped growth chambers. In short, each bacterium is represented by two point particles that repel each other by a growth force. After a critical size threshold is reached, the cell divides, and two new particles are added. To model the feedback on growth, the growth force is taken to be proportional to the nutrient uptake. Nutrients are supplied with constant density at the outlets and are consumed by the bacteria (for details of the simulation technique, see Material and methods). This model and simulation technique is also able to incorporate features currently not taken into account, such as the finite elasticity of bacteria or pressure-dependent growth, offering many possibilities for further studies. To demonstrate the predictive power of our simulation model, we calculate the time-dependent growth of bacteria inside a rectangular *growth chamber* with two narrow feeding outlets at both sides, as depicted in figure 1*a* and *c*, and compare our predictions with experimental results. In the experiments, we analyse spreading of a colony of *C. glutamicum* with prescribed feeding concentrations $g_\infty = 19.5\,\mu M$ $(n = 3)$ and $g_\infty = 195\,\mu M$ $(n = 7)$. A few bacteria are seeded in the growth chamber at $t = 0$, and subsequent colony spreading is observed via time-lapse imaging. Clearly, the spreading dynamics is very sensitive to the initial conditions. If initially all bacteria are concentrated at one spot, a single circular colony develops, whereas if the bacteria are initially distributed over the chamber, multiple separate colonies grow and finally merge (see figure 4*a*(i),*b*(i),*c*(i),*d*(i) and electronic supplementary material, figure S3). The simulations are initialized with the same amount of cells at identical positions as in the experiment. We convert the experimental feeding concentration g_∞ to simulation units via the previously calculated concentration scale $\bar{g}$. Visual comparison of the shape of the colony predicted by simulations and observed in experiments already shows excellent agreement, with growth patterns in nice synchrony (figure 4*a*(ii),*b*(ii),*c*(ii),*d*(ii)), especially for colonies larger than $A = 500\,\mu m^2$. Furthermore, the overall colony area $A(t)$ over time serves as an easily accessible quantifier for comparison (figure 4*a*(iii),*b*(iii),*c*(iii),*d*(iii)). The growth of colonies consisting of only a few bacteria depends strongly on the state of the cell cycle of every individuum, such that we expect a large variability in growth. Therefore, we expect that our model agrees best in the later stages of the experiment, when memory effects have worn out and the continuum description is appropriate. The simulation time axis is therefore shifted such that $A(t)$ coincides with the last data point of the experiment. For experiments with concentration $g_\infty = 195\,\mu M$ (i.e. half our ‘fitting concentration’), simulations agree very well with experiments even down to colonies consisting of only the few cells at the starting point of the experiment (figure 4*a*–*c*). When extrapolating to the much lower concentration $g_\infty = 19.5\,\mu M$ (figure 4*d*), simulations still agree remarkably well for colonies larger than about $500\,\mu m^2$. In experiments with very low nutrient concentrations ($g_\infty = 19.5\,\mu M$), bacteria initially grow faster than predicted. This may be due to cell-history effects from preculture, e.g. carbon storage, or effects from the differences in population densities present in growth-channel experiments versus the smaller initial density in growth-chamber experiments. A quantitative understanding of this effect requires a more detailed study in the future.

Furthermore, our observations suggest directed growth towards the channel inlets. While, initially, colonies grow in a more or less circular shape, some elongate over time. The effect is weak, and sometimes caused by previous wall contact. However, in some cases (right colony in figure 4*d* and electronic supplementary material, figure S3 (II) and (IV)) orientation towards the inlets is visible. This indicates that the nutrient gradients, as predicted by the local growth profile $u(g)$ (figure 4*a*(ii),*b*(ii),*c*(ii),*d*(ii)) of our model, directly affect the temporal expansion of the colony. However, these changes in shape are subtle and further quantitative analysis is required.

Simulations can be improved further when hindered diffusion through bacteria is considered. In our model, this can be accounted for in a coarse-grained manner by defining two different diffusion constants, D_{bulk} and D_{free} inside and outside of the colony, respectively. For a spatially changing diffusion coefficient, the $D\Delta g$ term in equation (2.1) has then to be replaced by $\nabla \cdot (D\nabla g) = D\Delta g + \nabla D \cdot \nabla g$. The agreement with experiments is best for $D_{free}/D_{bulk} \approx 1.25$, a surprisingly small impediment if the bacteria were considered as obstacles [28,29].

3. Conclusion

In summary, we have shown how microfluidic devices can be exploited to measure the effect of nutrient availability and limitation on growth and transport in bacterial microcolonies. With some simple assumptions, like diffusive transport and mass balancing, we are able to quantitatively model growth and uptake kinetics. Our results show that at low nutrient concentration gradients in growth develop rapidly after a critical cell-colony size is reached (figure 4), both in experiment and simulation. It would be interesting to extend

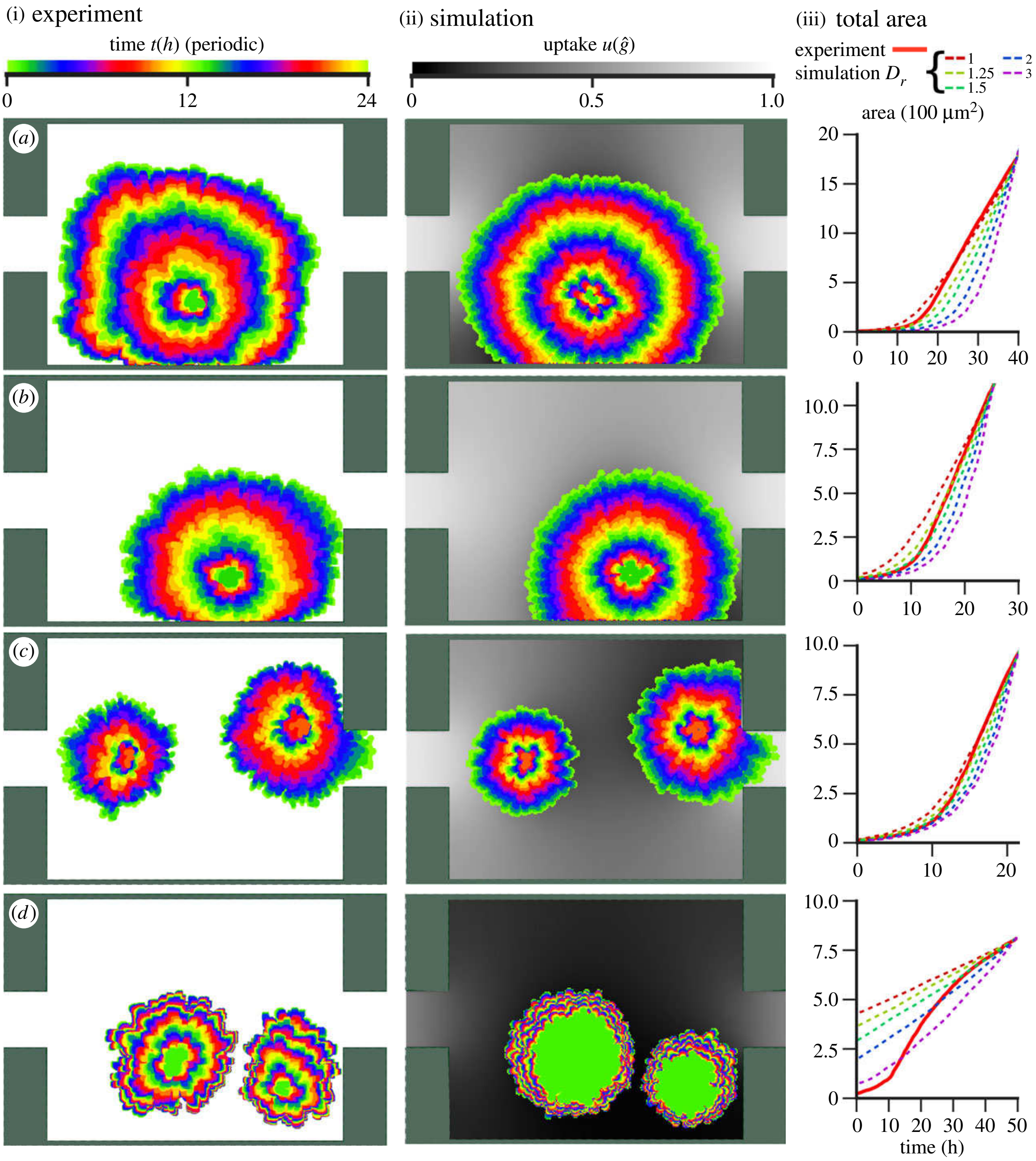

Figure 4. Dynamics of two-dimensional colony growth. Four examples of colony-spreading dynamics in simulation and experiment (see also the electronic supplementary material, movies M3–M6). Rows (*a*)–(*c*) belong to experiments with $g_\infty = 195$ µM while (*d*) shows an experiment with feeding concentration of $g_\infty = 19.5$ µM. (*a*(i),*b*(i),*c*(i),*d*(i)) Depiction of the colony shape dynamics in experiments. The outlines of the colony at equidistant time points are shown in different colours with a periodic colour scale (legend on top), 12 h have passed between two rings with the same colour. (*a*(ii),*b*(ii),*c*(ii),*d*(ii)) Same depiction as in the left column for outlines from the corresponding simulation with $D_{\mathrm{free}}/D_{\mathrm{bulk}} = 1.25$ (colourscale for outlines of the colony is the same as in the left column). The grey-shaded area around the colonies shows the profile of $u(g)$ at the last time point, illustrating the local limitation of growth due to nutrient depletion (legend on top). (*a*(iii),*b*(iii),*c*(iii),*d*(iii)) shows comparison of total colony area $A(t)$ in experiment (red line) and five corresponding simulations (dashed lines) with $D_r := D_{\mathrm{free}}/D_{\mathrm{bulk}} = 1, 1.25, 1.5, 2, 3$. The simulations have been shifted along the time axis such that they cross the last data point of the experiment (see electronic supplementary material, figure S5).

such studies to growth dynamics in the presence of antibiotics [30]. Furthermore, this approach should also work for eukaryotic and even mammalian cells and cell lines, where nutrient limitation can be of pivotal importance [4]. The modelling framework presented here can also be used and extended to optimize microfluidic geometries to guarantee and maintain optimal nutrient supply [18]. In particular, we hope that our results will stimulate a discussion about the existence and influence of environmental gradients within microfluidic cultivation systems. Our results can also serve as a basis for studies in related fields, such as the investigation of mechanical forces within cell growth and development [31–35]. Here, our approach could be used to quantitatively determine the effect of nutrient transport and limitation in order to extract the contribution of mechanical forces.

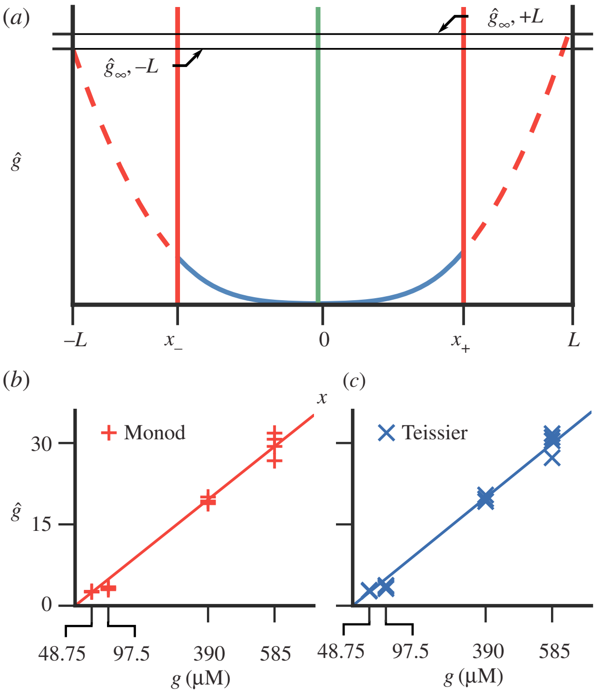

Figure 5. Extrapolation to $\hat{g}_\infty$. (*a*) Owing to the decreasing quality of the PIV data at the channel outlets, the model fit of the velocity profile is constrained to the data between the two points $x_\pm$ (red vertical lines). To get an estimate for $\hat{g}_\infty$, we solve the ode equation (4.1) for the concentration $\hat{g}$ (blue curve) with the fitted model parameters outside the range $x_- \le x \le x_+$ used for the fit (dashed red lines). Owing to the slight deviation of the fitted symmetry axis (green vertical) from the centre $x = 0$, the estimates for $\hat{g}_{\infty,\pm L}$ for $\hat{g}_\infty$ differ slightly. (*b*,*c*) Linear fit $\hat{g} = g/\bar{g}$ of the concentration $\hat{g}$ extrapolated at the channel outlets from our theory and the corresponding concentration in experiment g for Monod and Teissier uptake. (Online version in colour.)

4. Material and methods

4.1. Microbial strain and cultivation

Model organism in this study was *C. glutamicum* wild-type (ATCC 13032). Microfluidic cultivations were performed using two different cultivation chamber systems. For steady-state growth, a monolayer growth chamber as described by Mather *et al.* [17] was used, with a chamber dimension of 40 × 75 × 1 µm. For dynamical growth studies, the cultivation system described by [36] was applied. For chip fabrication details and further information the reader is referred to [36,37]. To prevent co-metabolism of different carbon sources [26], modified CGXII medium without glucose was used as the growth medium. Here protocatechuic acid (PCA) serves as a sole carbon source and was varied in concentration within the different sets of experiments. Modified CGXII medium was infused at approx. 200 nl min^{-1} after cell inoculation. Phase equilibrium experiments were performed as follows. First cells were cultivated at 10 × standard PCA concentration (195 µM) until chambers were filled; afterwards medium was switched to the desired concentration of PCA for steady-state experiments. Microfluidic pre-cultivation in 10 × PCA was chosen to 'equilibrate' cellular metabolism to the carbon source and to reduce the experimental time span for filling the microfluidic cultivation chambers. In the dynamic growth experiments (figure 4), cells were directly cultivated under the desired PCA concentration.

4.2. Live-cell imaging and analysis

The microfluidic chip was mounted onto a motorized inverted microscope (Nikon Eclipse Ti, Nikon microscopy, Germany) equipped with an incubator to keep the temperature at 30°. Time-lapse phase-contrast microscopy images of the growing microcolonies were recorded every 5–10 min for the growth channel experiments and every 30 min for the colony-spreading experiments over 50 h of microfluidic cultivation. After the microfluidic cultivation, chambers were manually inspected and selected for analysis. Recordings, in which fabrication inaccuracies led to unstable steady-state growth or steady-state growth in which differentiation of single cells was not possible anymore, were not further processed. Afterwards, we used the ImageJ PIV plugin implemented by Tseng [38] to quantify the velocity field in steady-state experiments. In dynamic growth experiments, the total area has been identified using the 'Auto Threshold'-Plugin in ImageJ to identify the outline of the bacterial colony. Hereby, small void spaces inside the colony are also added up to the total area. Measurements of the total area occupied by the colony have been performed in simulations by subdivision of the simulation domain in a two-dimensional grid and checking which lattice sides were occupied by at least one cell. We chose quarter the radius of the repulsive interaction between particles as the grid constant. We applied a binary closing on the resulting occupation matrix to close small holes inside of the occupation matrix. The area was then defined as the number of occupied lattice sites in the resulting matrix.

4.3. Fitting procedure

To extract values for the model parameters, namely maximum growth rate $k_{\max} = \epsilon u_\infty$ and nutrient diffusion length scale l_g, we fit our model equations (2.3) to the velocity profiles $v^{\exp}$ measured in experiments. For the uptake function, we tested two different models: Monod uptake [21] $u(\hat{g}) = \hat{g}/(1 + \hat{g})$ and Teissier uptake [22] $u(\hat{g}) = 1 - \exp(-\hat{g})$. In one dimension, equations (2.3) read

$$\hat{g}'' = \frac{u(\hat{g})}{l_g^2} \tag{4.1}$$

and

$$v' = k_{\max} u(\hat{g}), \tag{4.2}$$

with the prime denoting spatial derivatives. Insertion of $u(\hat{g})$ from equation (4.1) into the equation for v (4.2) leads to

$$v' = k_{\max} l_g^2 \hat{g}''.$$

Owing to the mirror symmetry around the channel centre $x_0 := 0$ of our set-up, the boundary conditions read $v(x_0) = \hat{g}'(x_0) = 0$. Integrating once, we obtain

$$v(x) = k_{\max} l_g^2 \hat{g}'(x). \tag{4.3}$$

We integrate equation (4.1) by using the `odeint()` method of the python package SciPy [39]. The corresponding velocity profile is then given according to equation (4.3). We fit the model solution for the velocity profile to the velocity profiles $v^{\exp}$ measured in the experiments by means of a least-squares optimization. To avoid confusion, we enumerate quantities belonging to different experiments with a superscript *i* in the following, e.g. $v^{\exp,i}$ denotes the velocity profile of experiment *i*. We define the cost function Π by the sum of the squared deviations at all points x_j^i within the fit range measured in experiments:

$$\Pi = \sum_{ij} \left[v^{\exp,i}(x_j^i) - k_{\max} l_g^2 \frac{\mathrm{d}\hat{g}^i}{\mathrm{d}x}(x_j^i) \right]^2. \tag{4.4}$$

To account for small deviations of the symmetry axis of the experimental flow profiles from the channel centre the positions x_0^i are also free fit parameters. Resulting symmetry axis positions x_0^i deviate only slightly from the channel centre with a relative error $x_0/2L < 2.5\%$. We minimize the cost function Π with respect to the parameter l_g, the prefactor $\lambda := k_{\max} l_g^2$ of g' in equation (4.4), and the set of symmetry axis positions $\{x_0^i\}$ and

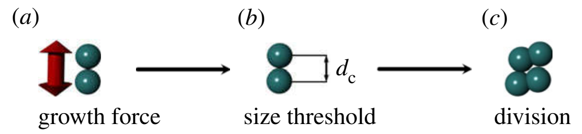

Figure 6. Schematic of the growth model in simulations. (*a*) Every cell consists of two point particles which interact with particles of other cells with a purely repulsive interaction, the excluded volume being indicated by spheres. Particles of the same cell repel each other with a growth force $F_g = B/(r + r_0)^2$ until a size threshold d_c is reached. (*b*,*c*) At the size threshold a cell divides: two new daughter cells are placed in close proximity to the mother cell particles. The growth force strength B is proportional to the local nutrient uptake (see equation (4.6)) to achieve nutrient-dependent growth. (Online version in colour.)

central concentrations $\{\hat{g}(x_0^i)\}$. Thus, for a set of N experiments the fit parameter space is of dimensionality $2 + 2N$. Minimization is performed with the `least_squares()` method of the SciPy python package [39].

As discussed in the main text, the three independent experiments belonging to the PCA concentration $g_\infty = 390\,\mu\text{M}$ cover almost the complete range of the uptake function as can be seen in figure 3. To probe the validity of our model, we estimate the model parameters l_g and $k_{\max}$ using these experiments, and extrapolate to all other experiments. In the remaining experiments only the symmetry points $\{x_0^i\}$ and central concentrations $\{\hat{g}(x_0^i)\}$ are obtained by minimization.

With the optimal fit solutions for the concentrations $\hat{g}$ at hand, we can estimate the remaining physical parameter, the concentration scale $g_{1/2}$ at which growth and uptake are at half their maximum values. To calculate these values in physical units, we need to estimate the concentration scale $\bar{g}$ which links between dimensionless theory concentrations $\hat{g}$ and experimental concentrations g via $\hat{g} = g/\bar{g}$. We estimate $\bar{g}$ by comparison of the feeding concentrations g_∞ present at the channel entries and their model prediction $\hat{g}_\infty$. We calculate $\hat{g}_\infty$ by extrapolation of the concentration profile g towards the channel entries at $x = \pm L$ (figure 5). We expect that this extrapolation only results in coarse estimates for the concentrations g_∞ because our model is not strictly valid at the channel entries due to reduced bacterial density. Furthermore, due to the slight deviation of the fitted symmetry axis position x_0^i from the channel centre at $x = 0$, the extrapolation results in two different concentration values at the entries at $x = \pm L$. We define $\hat{g}_\infty$ as their mean. The extrapolated concentration values $\hat{g}_\infty$ show a good agreement with a linear fit $\hat{g} = g/\bar{g}$ as depicted in figure 5*b*,*c*. The good match of experimental and theoretical concentrations provides thus an additional consistency check for our model. Table 1 shows a summary of all model parameters resulting from our fitting procedure using Monod or Teissier uptake.

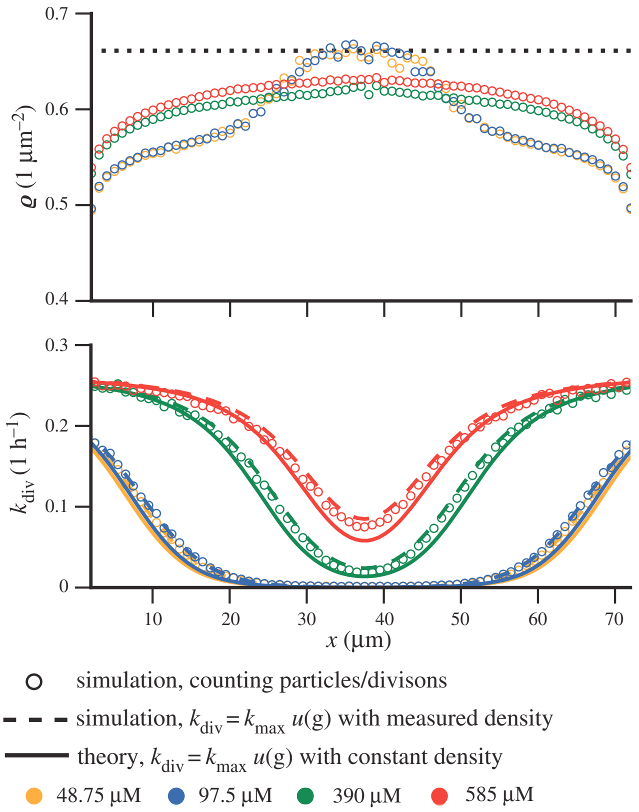

Figure 7. Number density and division rate in simulations. (*a*) Number density profiles ϱ for steady-state simulations at different feeding concentrations (different colours correspond to different concentrations; see legend at bottom). Horizontal dotted line depicts density value of $\varrho = 0.66\,\mu\text{m}^{-2}$ used to calculate the uptake rate $u_\infty = D/l_g^2\varrho$ for the simulations from the fitted value for l_g^2. (*b*) Division rate $k_{\rm div}$, directly measured during simulation by counting division events (empty circles), from $k_{\rm div} = k_{\max}u(\hat{g}(x))$ with $\hat{g}(x)$ measured in simulations (dashed lines) and as predicted by the theoretical model assuming constant density (continuous lines). Depicted results for number density and division rate have been obtained by averaging over time and along the *y*-direction. (Online version in colour.)

4.4. Simulation model

We base our simulation on the previously published particle-based model used to study the dynamics of growing systems in various contexts [23,33,40,41]. In this model, cells consist of two particles that separate due to a repulsive growth force $F_g = B/(r + r_0)^2$, with force constants B and r_0 (figure 6). Additionally, a friction force between the two cell particles $\boldsymbol{F}_c = -\gamma_c \boldsymbol{v}_c$ is added, with $\boldsymbol{v}_c$ denoting the relative velocity of the particles constituting one cell. At a given size threshold d_c the cell divides, and two new daughter cells are placed in close proximity to the mother cell. The friction constant γ_c is chosen large enough to result in overdamped growth dynamics. Intracell noise is added in a Brownian dynamics fashion [42]; we denote the corresponding diffusion constant by D_c. The division time of an isolated cell $\tau_{\rm div}^{\rm sim}$ is then given by

$$\tau_{\rm div}^{\rm sim} = \frac{\gamma_c}{B}\int_0^{d_c} (r + r_0)^2\,\mathrm{d}r. \qquad (4.5)$$

Two particles at positions $\boldsymbol{r}_i$ and $\boldsymbol{r}_j$ with $r_{ij} = |\boldsymbol{r}_i - \boldsymbol{r}_j|$, belonging to different cells, interact with each other with a force of magnitude $F_{cc} = f_0(1/r_{ij}^5 - 1) - f_1$ directed along the unit vector $\hat{r}_{ij} = (r_i - r_j)/r_{ij}$. In this study, we set the attractive component to zero, i.e. $f_1 = 0$ for all simulations. Dissipation and fluctuation forces between particles of different cells are modelled according to the dissipative particle dynamics technique [42], the corresponding friction constant and diffusion constant are denoted by γ_t and D_t, respectively. A background friction force $\boldsymbol{F}_b = -\gamma_b \boldsymbol{v}$ with friction constant γ_b and $\boldsymbol{v}$, the velocity in the laboratory coordinate system, acts on all particles. The corresponding background noise is modelled in a Brownian dynamics fashion [42] with diffusion constant D_b. All forces are cut-off at a cut-off radius $r_{\rm cut} = 1.1\,\mu\text{m}$. We set the diffusion constants $D_{b,c,t}$ of all particle–particle interactions to $1.21 \times 10^{-3}\,\mu\text{m}^2\,\text{h}^{-1}$.

We integrate the nutrient dynamic equation (2.1) on a square lattice $(x_i, y_j) = h(i, j)$ with lattice constant $h = 1\,\mu\text{m}$. We employ a forward-time, central-space finite-difference scheme taking into account spatial varying diffusion constants [43]. In the following, we denote quantities estimated at grid site (x_i, y_j) in simulations with a subscript ij, e.g. the concentration $\hat{g}_{ij} = \hat{g}(x_i, y_j)$. We set the

Table 2. Summary of simulation parameters. Forces are given relative to the background friction constant γ_b.

parameter	value	description
dt_{DPD}	5×10^{-5} h	DPD-integration timestep
h	1 µm	finite-difference grid constant
dt_{FD}	10^{-5} h	finite-difference timestep
r_0	1.1 µm	growth pressure constant
r_{cut}	1.1 µm	cut-off radius of all pair-potentials
d_c	1.1 µm	size threshold for cell division
r_c	1.1×10^{-5} µm	distance at which new particles are placed after division
D_b	1.21×10^{-3} µm^2 h^{-1}	background noise diffusion constant of bacteria
D_t	1.21×10^{-3} µm^2 h^{-1}	intercell noise diffusion constant of bacteria
D_c	1.21×10^{-3} µm^2 h^{-1}	intracell noise diffusion constant of bacteria
γ_t/γ_b	1	intercell friction constant
γ_c/γ_b	10^4	intracell friction constant
f_0/γ_b	460 µm h^{-1}	repulsive force constant
f_1/γ_b	0 µm h^{-1}	attractive force constant
D_{bulk}	2478(1888) µm^2 h^{-1}	nutrient diffusion constant inside colony for Monod (Teissier) uptake

diffusion constant equal to D_{free} at every lattice site with no cell inside and to a smaller value $D_{\mathrm{bulk}} \leq D_{\mathrm{free}}$ at every site with at least one cell present. This models the hindered diffusion of nutrient molecules around and through the cell membrane in a coarse-grained manner. Analytical calculations in [28,29] provide the expression $D_{\mathrm{bulk}} = D_{\mathrm{free}}((1-\nu)/(1+\nu))$ for a two-dimensional array of impermeable cylinders with packing fraction ν. The packing fraction of bacteria of approx. $\nu \approx 0.5$ thus results in $D_{\mathrm{bulk}}/D_{\mathrm{free}} = \frac{1}{3}$. The local cell density ϱ_{ij} is obtained from the centre of mass coordinates of cells binned on the lattice. The cell density ϱ_{ij} is used to calculate the local uptake rate $u_\infty \varrho_{ij} u(\hat{g}_{ij})$ which enters the diffusion equation (2.1). We confirmed consistency of results with double or half the grid constant h and agreement with analytical solutions of the one-dimensional equation (4.1).

To transfer the diffusion length scale l_g from our model fit to simulations, we choose $u_\infty = D_{\mathrm{bulk}}/(l_g^2 \varrho_{\mathrm{exp.}})$ with $\varrho_{\mathrm{exp.}} = 0.66$ µm^{-2}. As the diffusion constant D_{PCA} of our limiting factor PCA is of the order of 100 µm^2 s^{-1} [44], the concentration profile equilibrates in a timespan $\tau_{\mathrm{diff}} = L^2/D$ on the order of seconds. As bacteria move with a few µm h^{-1} and divide on a timescale of $\tau_{\mathrm{div}} = 1/k_{\max} = 3-4$ h, the timescale of bacterial dynamics τ_{bact} is on the order of a few hours. Thus, the concentration profile equilibrates almost instantly on the timescale of bacterial dynamics. Hence, in simulations, it is not necessary to set exactly $D_{\mathrm{free}} = D_{\mathrm{PCA}}$, any value of D_{free} large enough such that $\tau_{\mathrm{diff}} \ll \tau_{\mathrm{bact}}$ will result in the same bacterial dynamics (as long as u_∞ is scaled accordingly). For numerical efficiency we choose diffusion constants $D_{\mathrm{bulk}} = 2478$ µm^2 h^{-1} ($D_{\mathrm{bulk}} = 1888$ µm^2 h^{-1} for Teissier uptake), large enough such that $\tau_{\mathrm{diff}} \ll \tau_{\mathrm{div}}$.

To reproduce the local growth rate $k_g = k_{\max} u(\hat{g})$ of bacteria (see equation (2.3)) in simulations, we let the growth force constant B depend on the local uptake $u(\hat{g})$ (compare equation (4.5))

$$B(\hat{g}) = \frac{\gamma_c k_{\max} u(\hat{g})}{\log(2)} \int_0^{d_c} (r + r_0)^2 \, \mathrm{d}r. \tag{4.6}$$

Note that expression (4.5) is only valid if the growth force scale B is much larger than the pressure forces the cells are exposed to in the bulk. We can estimate these forces by considering the force balance equation $p' = -\varrho \gamma_b v$ in our one-dimensional model. With vanishing pressure at the channel entries $x = \pm L$ the maximum pressure in the channel centre scales with $p \sim \varrho k_{\max} \gamma_b L^2$. For the set of simulations as presented in the main text, we aim to stay close to the dynamics as described by model equations (2.1) and (2.2) and choose γ_c such that $B(g) \gg \varrho k_{\max} \gamma_b L^2$, i.e. growth is pressure independent.[1] The smooth repulsion potentials result in a non-zero compressibility K scaling with the repulsive force constant $1/K \sim f_0$. Therefore, the number density increases towards the channel centre where pressure is largest (figure 7*a*). Owing to the non-constant bacterial density ϱ in simulations the concentration profile in simulations is not exactly given by the solution of model equation (2.1) which assumes constant density. As the concentration profile enters in equation (4.6) to determine the local growth rate, model and simulation division rate agree only if the repulsive force constant f_0 is large enough to result in only small variations of the number density around ϱ_{exp}. For the simulations as presented in the main text, we choose a rather large repulsive force constant of $f_0/\gamma_b = 460$ µm h^{-1}. Thus, separate measurements of the division rate confirm the match between model and simulation (figure 7*b*).

We also performed growth channel simulations with softer cells and pressure-dependent growth which resulted in velocity profiles similarly to those presented in figure 2*a*. However, the match of feeding concentrations in simulations and experiment, as expressed in the linear relationship $\hat{g} = g/\bar{g}$ in figure 5*b*,*c*, had a larger error. All simulation parameters are summarized in table 2.

Data accessibility. Relevant experimental and simulation data are available in an external repository, (doi:10.5281/zenodo.998797) [46].

Authors' contributions. J.E., A.G., R.H., D.K. and G.G. designed the research; R.H., J.E. performed data analysis and theoretical modelling; A.G. and C.W. performed the experiment and image analysis. All authors discussed the results and wrote the paper.

Competing interests. We declare we have no competing interests.

Funding. Alexander Grünberger (PD-311) and Dietrich Kohlheyer (VH-NG-1029) are financially supported by the Helmholtz Association.

Acknowledgements. Raphael Hornung acknowledges support by the International Helmholtz Research School of Biophysics and Soft Matter (IHRS BioSoft). Microfabrication was performed at Helmholtz Nanoelectronic Facility (HNF) of Forschungszentrum Jülich [47]. The authors gratefully acknowledge a computing-time grant on the supercomputer JURECA at Jülich Supercomputing Centre (JSC [48]). We thank Sebastian Schmidt for initiating the cooperation between the institutes IBG-1 and ICS-2.

Endnote

[1] If the scales of local pressure and growth pressure are comparable, growth behaves according to the *homeostatic pressure model* with a growth rate $k_g \propto p_h - p$, p_h being a species-dependent constant called the homeostatic pressure [23,45].

References

1. Wang P, Robert L, Pelletier J, Dang WL, Taddei F, Wright A, Jun S. 2010 Robust growth of escherichia coli. *Curr. Biol.* **20**, 1099–1103. (doi:10.1016/j.cub.2010.04.045)
2. Taheri-Araghi S, Bradde S, Sauls JT, Hill NS, Levin PA, Paulsson J, Vergassola M, Jun S. 2015 Cell-size control and homeostasis in bacteria. *Curr. Biol.* **25**, 385–391. (doi:10.1016/j.cub.2014.12.009)
3. Gospodarowicz D, Moran JS. 1976 Growth factors in mammalian cell culture. *Annu. Rev. Biochem.* **45**, 531–558. (doi:10.1146/annurev.bi.45.070176.002531)
4. Hirschhäuser F, Menne H, Dittfeld C, West J, Mueller-Klieser W, Kunz-Schughart LA. 2010 Multicellular tumor spheroids: an underestimated tool is catching up again. *J. Biotechnol.* **148**, 3–15. (doi:10.1016/j.jbiotec.2010.01.012)
5. Rumpler M, Woesz A, Dunlop JW, van Dongen JT, Fratzl P. 2008 The effect of geometry on three-dimensional tissue growth. *J. R. Soc. Interface* **5**, 1173–1180. (doi:10.1098/rsif.2008.0064)
6. Lovett M, Lee K, Edwards A, Kaplan DL. 2009 Vascularization strategies for tissue engineering. *Tissue Eng. Part B Rev.* **15**, 353–370. (doi:10.1089/ten.TEB.2009.0085)
7. Huh D, Hamilton GA, Ingber DE. 2011 From 3D cell culture to organs-on-chips. *Trends Cell. Biol.* **21**, 745–754. (doi:10.1016/j.tcb.2011.09.005)
8. Bhatia SN, Ingber DE. 2014 Microfluidic organs-on-chips. *Nat. Biotechnol.* **32**, 760–772. (doi:10.1038/nbt.2989)
9. Donlan RM. 2002 Biofilms: microbial life on surfaces. *Emerg. Infect. Dis.* **8**, 881–890. (doi:10.3201/eid0809.020063)
10. Stewart PS. 2003 Diffusion in biofilms. *J. Bacteriol.* **185**, 1485–1491. (doi:10.1128/JB.185.5.1485-1491.2003)
11. Wilking JN, Angelini TE, Seminara A, Brenner MP, Weitz DA. 2011 Biofilms as complex fluids. *MRS Bull.* **36**, 385–391. (doi:10.1557/mrs.2011.71)
12. Liu J, Prindle A, Humphries J, Gabalda-Sagarra M, Asally M, Lee DyD, Ly S, Garcia-Ojalvo J, Süel GM. 2015 Metabolic co-dependence gives rise to collective oscillations within biofilms. *Nature* **523**, 550–554. (doi:10.1038/nature14660)
13. Whitesides GM. 2006 The origins and the future of microfluidics. *Nature* **442**, 368–373. (doi:10.1038/nature05058)
14. Grünberger A, Wiechert W, Kohlheyer D. 2014 Single-cell microfluidics: opportunity for bioprocess development. *Curr. Opin. Biotechnol.* **29**, 15–23. (doi:10.1016/j.copbio.2014.02.008)
15. Schmid A, Kortmann H, Dittrich PS, Blank LM. 2010 Chemical and biological single cell analysis. *Curr. Opin. Biotechnol.* **21**, 12–20. (doi:10.1016/j.copbio.2010.01.007)
16. Kortmann H, Blank LM, Schmid A. 2011 *Single cell analytics: an overview*, pp. 99–122. Berlin, Germany: Springer. (doi:10.1007/10_2010_96)
17. Mather W, Mondragón-Palomino O, Danino T, Hasty J, Tsimring LS. 2010 Streaming instability in growing cell populations. *Phys. Rev. Lett.* **104**, 208101. (doi:10.1103/PhysRevLett.104.208101)
18. Westerwalbesloh C, Grünberger A, Stute B, Weber S, Wiechert W, Kohlheyer D, von Lieres E. 2015 Modeling and cfd simulation of nutrient distribution in picoliter bioreactors for bacterial growth studies on single-cell level. *Lab Chip* **15**, 4177–4186. (doi:10.1039/C5LC00646E)
19. Cherifi T, Jacques M, Quessy S, Fravalo P. 2017 Impact of nutrient restriction on the structure of listeria monocytogenes biofilm grown in a microfluidic system. *Front. Microbiol.* **8**, 864. (doi:10.3389/fmicb.2017.00864)
20. Grünberger A, Paczia N, Probst C, Schendzielorz G, Eggeling L, Noack S, Wiechert W, Kohlheyer D. 2012 A disposable picolitre bioreactor for cultivation and investigation of industrially relevant bacteria on the single cell level. *Lab Chip* **12**, 2060–2068. (doi:10.1039/c2lc40156h)
21. Monod J. 1949 The growth of bacterial cultures. *Annu. Rev. Microbiol.* **3**, 371–394. (doi:10.1146/annurev.mi.03.100149.002103)
22. Teissier G. 1938 Les lois quantitatives de la croissance. *Ann. Physiol. Physicochim. Biol.* **12**, 527–586.
23. Basan M, Prost J, Joanny JF, Elgeti J. 2011 Dissipative particle dynamics simulations for biological tissues: rheology and competition. *Phys. Biol.* **8**, 026014. (doi:10.1088/1478-3975/8/2/026014)
24. Farrell FDC, Hallatschek O, Marenduzzo D, Waclaw B. 2013 Mechanically driven growth of quasi-two-dimensional microbial colonies. *Phys. Rev. Lett.* **111**, 168101. (doi:10.1103/PhysRevLett.111.168101)
25. Melaugh G, Hutchison J, Kragh KN, Irie Y, Roberts A, Bjarnsholt T, Diggle SP, Gordon VD, Allen RJ. 2016 Shaping the growth behaviour of biofilms initiated from bacterial aggregates. *PLoS ONE* **11**, e0149683. (doi:10.1371/journal.pone.0149683)
26. Unthan S, Grünberger A, van Ooyen J, Gätgens J, Heinrich J, Paczia N, Wiechert W, Kohlheyer D, Noack S. 2014 Beyond growth rate 0.6: What drives Corynebacterium glutamicum to higher growth rates in defined medium. *Biotechnol. Bioeng.* **111**, 359–371. (doi:10.1002/bit.25103)
27. Raffel M, Willert C, Wereley S, Kopenhans J. 1998 *Particle image velocimetry—A Practical Guide*, pp. 1–448. Berlin, Germany: Springer.
28. Ochoa-Tapia JA, Stroeve P, Whitaker S. 1994 Diffusive transport in two-phase media: spatially periodic models and Maxwell's theory for isotropic and anisotropic systems. *Chem. Eng. Sci.* **49**, 709–726. (doi:10.1016/0009-2509(94)85017-8)
29. Wood BD, Quintard M, Whitaker S. 2002 Calculation of effective diffusivities for biofilms and tissues. *Biotechnol. Bioeng.* **77**, 495–516. (doi:10.1002/bit.10075)
30. Allen R, Waclaw B. 2016 Antibiotic resistance: a physicist's view. *Phys. Biol.* **13**, 045001. (doi:10.1088/1478-3975/13/4/045001)
31. Montel F *et al.* 2011 Stress clamp experiments on multicellular tumor spheroids. *Phys. Rev. Lett.* **107**, 188102. (doi:10.1103/PhysRevLett.107.188102)
32. Grant MAA, Wacław B, Allen RJ, Cicuta P. 2014 The role of mechanical forces in the planar-to-bulk transition in growing escherichia coli microcolonies. *J. R. Soc. Interface* **11**, 20140400. (doi:10.1098/rsif.2014.0400)
33. Podewitz N, Delarue M, Elgeti J. 2015 Tissue homeostasis: a tensile state. *Europhys. Lett.* **109**, 58005. (doi:10.1209/0295-5075/109/58005)
34. Delarue M, Hartung J, Schreck C, Gniewek P, Hu L, Herminghaus S, Hallatschek O. 2016 Self-driven jamming in growing microbial populations. *Nat. Phys.* **12**, 762–766. (doi:10.1038/nphys3741)
35. Farrell FD, Gralka M, Hallatschek O, Waclaw B. 2017 Mechanical interactions in bacterial colonies and the surfing probability of beneficial mutations. *J. R. Soc. Interface* **14**, 20170073. (doi:10.1098/rsif.2017.0073)
36. Grünberger A *et al.* 2015 Spatiotemporal microbial single-cell analysis using a high-throughput microfluidics cultivation platform. *Cytometry A* **87**, 1101–1115. (doi:10.1002/cyto.a.22779)
37. Grünberger A, Probst C, Heyer A, Wiechert W, Frunzke J, Kohlheyer D. 2013 Microfluidic picoliter bioreactor for microbial single-cell analysis: fabrication, system setup, and operation. *J. Vis. Exp.* **82**, e50560. (doi:10.3791/50560)
38. Tseng Q, Duchemin-Pelletier E, Deshiere A, Balland M, Guillou H, Filhol O, Théry M. 2012 Spatial organization of the extracellular matrix regulates cell–cell junction positioning. *Proc. Natl Acad. Sci. USA* **109**, 1506–1511. (doi:10.1073/pnas.1106377109)
39. Oliphant TE. 2007 Python for scientific computing. *Comput. Sci. Eng.* **9**, 10–20. (doi:10.1109/MCSE.2007.58)
40. Montel F, Delarue M, Elgeti J, Vignjevic D, Cappello G, Prost J. 2012 Isotropic stress reduces cell proliferation in tumor spheroids. *New J. Phys.* **14**, 055008. (doi:10.1088/1367-2630/16/11/115005)
41. Marel AK, Podewitz N, Zorn M, Rädler JO, Elgeti J. 2014 Alignment of cell division axes in directed epithelial cell migration. *New J. Phys.* **16**, 115005. (doi:10.1088/1367-2630/16/11/115005)
42. Frenkel D, Smit B. 2001 *Understanding molecular simulation: from algorithms to applications*, 2nd edn. London, UK: Academic Press.
43. Strikwerda J. 2004 *Finite difference schemes and partial differential equations*, p. 163, eq. (6.5.1), 2nd edn. Philadelphia, PA: Society for Industrial and Applied Mathematics. (doi:10.1137/1.9780898717938)

44. Srinivas K, King JW, Howard LR, Monrad JK. 2011 Binary diffusion coefficients of phenolic compounds in subcritical water using a chromatographic peak broadening technique. *Fluid Phase Equilibr*. **301**, 234 – 243. (doi:10.1016/j.fluid.2010.12.003)
45. Basan M, Risler T, Joanny JF, SastreGarau X, Prost J. 2009 Homeostatic competition drives tumor growth and metastasis nucleation. *HFSP J.* **3**, 265 – 272. (doi:10.2976/1.3086732)
46. Hornung R, Grünberger A, Westerwalbesloh C, Kohlheyer D, Gompper G, Elgeti J. 2017 Quantitative modelling of nutrient-limited growth of bacterial colonies in microfluidic cultivation. [Data set]. Zenodo (doi:10.5281/zenodo.998797)
47. Forschungszentrum Jülich GmbH. 2017 HNF-Helmholtz nano facility. *J. Large Scale Res. Facil.* **3**, A112. (doi:10.17815/jlsrf-3-158)
48. Jülich Supercomputing Centre. 2016 JURECA: general-purpose supercomputer at Jülich Supercomputing Centre. *J. Large Scale Res. Facil.* **2**, A62. (doi:10.17815/jlsrf-2-121)